2 mm GISMO Observations of the Galactic Center. I. Dust Emission[*]

Richard G. Arendt[1,2] , Johannes Staguhn[1,3] , Eli Dwek[1] , Mark R. Morris[4] , Farhad Yusef-Zadeh[5], Dominic J. Benford[6] ,
Attila Kovács[7] , and Junellie Gonzalez-Quiles[8,9]

[1] Code 665, NASA/GSFC, 8800 Greenbelt Road, Greenbelt, MD 20771, USA; Richard.G.Arendt@nasa.gov, Johannes.G.Staguhn@nasa.gov, Eli.Dwek@nasa.gov
[2] CRESST2/UMBC, USA
[3] Johns Hopkins University, USA
[4] Department of Physics and Astronomy, University of California Los Angeles, Los Angeles, CA 90095, USA; morris@astro.ucla.edu
[5] CIERA and the Department of Physics & Astronomy, Northwestern University, 2145 Sheridan Road, Evanston, IL 60208, USA; zadeh@northwestern.edu
[6] Astrophysics Division, NASA Headquarters, 300 E Street SW, Washington, DC 20546, USA; Dominic.J.Benford@nasa.gov
[7] Smithsonian Astrophysical Observatory Submillimeter Array (SMA), MS-78, 60 Garden Street, Cambridge, MA 02138, USA; attila.kovacs@cfa.harvard.edu
[8] Code 667, NASA/GSFC, 8800 Greenbelt Road, Greenbelt, MD 20771, USA; Junellie.Gonzalez-Quiles@nasa.gov
[9] CRESST2/SURA, USA

Abstract

The central molecular zone, covering the inner $\sim$1° of the Galactic plane has been mapped at 2 mm using the Goddard-IRAM Superconducting 2-Millimeter Observer (GISMO) bolometric camera on the 30 m IRAM telescope. The 21″ resolution maps show abundant emission from cold molecular clouds, from star-forming regions, and from one of the Galactic center nonthermal filaments. In this work we use the *Herschel* Hi-GAL data to model the dust emission across the Galactic center. We find that a single-temperature fit can describe the 160–500 μm emission for most lines of sight, if the long-wavelength dust emissivity scales as $\lambda^{-\beta}$ with $\beta \approx 2.25$. This dust model is extrapolated to predict the 2 mm dust emission. Subtraction of the model from the GISMO data provides a clearer look at the 2 mm emission of star-forming regions and the brightest nonthermal filament.

Unified Astronomy Thesaurus concepts: Interstellar dust (836); Dust continuum emission (412); Far infrared astronomy (529); Millimeter astronomy (1061); Galactic center (565); Radio continuum emission (1340)

1. Introduction

The Galactic center presents an interesting challenge to observe and understand because of the huge variety of sources and structures that are superimposed along the line of sight. The line-of-sight extinction prevents any useful observations at UV or optical wavelengths. The development of infrared, radio, and X-ray observations has provided a clearer view of the Galactic center region. Infrared and radio observations have revealed the central molecular zone (CMZ) within Galactic longitude $|l| \lesssim 1$° or a radius of $\sim$140 pc of the Galactic center (Morris & Serabyn 1996). The CMZ contains the largest, densest collection of giant molecular clouds in the Galaxy. Originating from these clouds are numerous star-forming regions and young stellar objects with various sizes and ages (e.g., Yusef-Zadeh et al. 2009). These in turn have generated large stellar clusters, including the nuclear cluster that swarms around the Galaxy's central supermassive black hole, and the more outlying Arches and Quintuplet Clusters (e.g., Figer et al. 1999, 2002; Genzel et al. 2003). The clusters and individual stars interact with their surrounding medium to produce ionized structures and bubbles (Simpson et al. 1997; Cotera et al. 2005; Simpson et al. 2007). Nonthermal radio structures are seen in the form of supernova remnants and an assortment of individual and bundles of filaments. High-energy (X-ray) observations (e.g., Wang et al. 2002) reveal emission from sources such as accreting compact objects (white dwarfs, neutron stars, or stellar-mass black holes) in binary systems, very hot gas, and colliding stellar winds (Wang et al. 2006;

Yusef-Zadeh et al. 2015). Figure 1 provides a guide to the locations of some of the relevant structures in the CMZ.

New observations with new instruments invariably provide insight to one or more of these components of the Galactic center region. We have carried out a 2 mm continuum survey of the CMZ region using the IRAM 30 m telescope (Baars et al. 1987) paired with the Goddard-IRAM Superconducting 2-Millimeter Observer (GISMO) instrument (Staguhn et al. 2006; Staguhn et al. 2008). Observations at 2 mm are in an interesting transition zone between mid- and far-IR wavelengths on the one hand (10–500 μm), which are generally dominated by emission from warm and cold interstellar dust, and radio wavelengths on the other hand ($>$1 cm), where the dominant emission mechanisms are free–free emission from ionized gas and synchrotron emission from relativistic electrons. The GISMO survey offers coverage of a wide angular extent (the entire CMZ) with excellent sensitivity and the ability to trace large angular scale emission that higher angular resolution interferometric observations miss. Previous similar surveys and observations are the BOLOCAM Galactic Plane Survey (Bally et al. 2010; Ginsburg et al. 2013), which covers the entire CMZ at 1.1 mm and is thus dominated by cold dust emission; 3 mm interferometric observations of the inner portion of the CMZ from Sgr A to the Radio Arc by Pound & Yusef-Zadeh (2018), which are sensitive to thermal and nonthermal radio emission and very insensitive to thermal dust emission; 2 mm observations of the Radio Arc region by Reich et al. (2000); and relatively low angular resolution observations at 2 and 3 mm (and other wavelengths) by cosmic microwave background surveys (Culverhouse et al. 2010; Planck Collaboration et al. 2015).
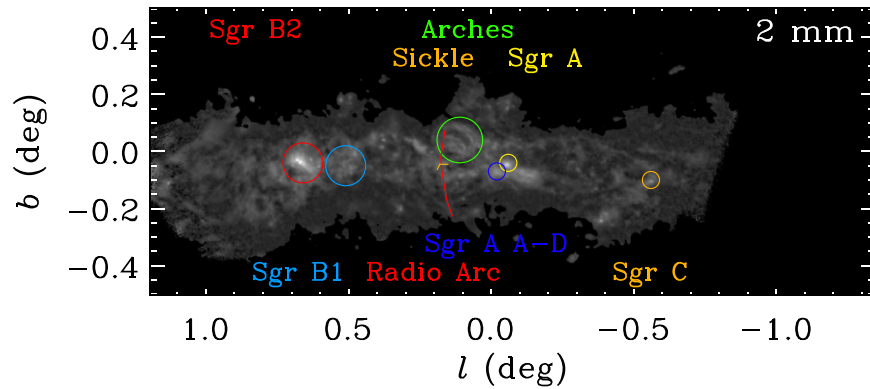

Figure 1. Features in the CMZ. Originally defined from longer-wavelength radio observations, these features are notable 2 mm sources as well. See Figure 4 for an unadorned version of the 2 mm image.
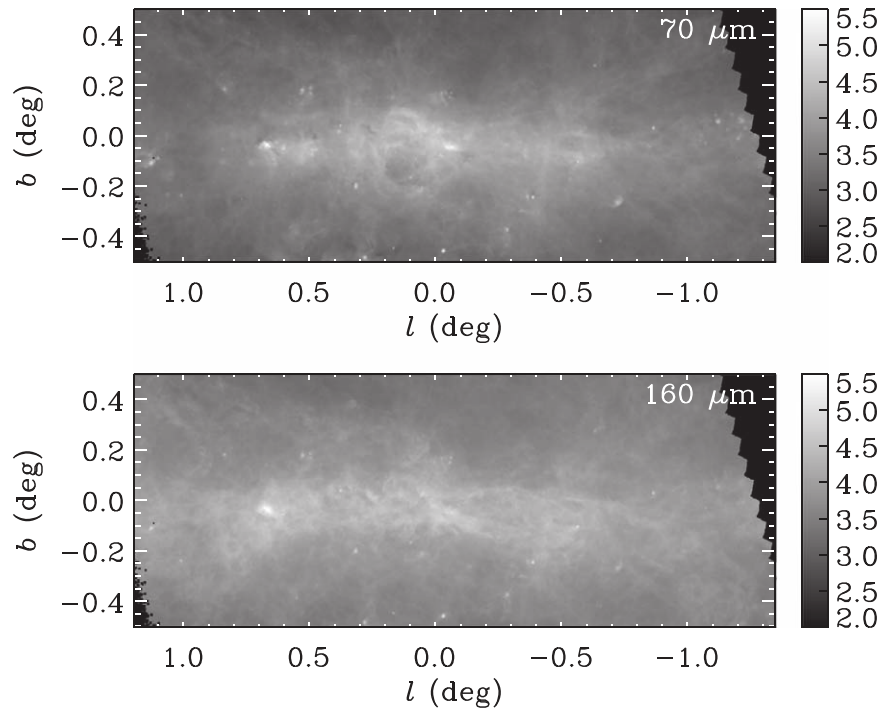

Figure 2. *Herschel* PACS 70 (top) and 160 μm (bottom) images from the Hi-GAL survey (Molinari et al. 2016). These are displayed on a logarithmic scale spanning $[100, 3.5 \times 10^5]$ MJy sr^{-1}. These images are convolved to the 21″ resolution of the GISMO 2 mm data. Emission is dominated by cool dust ($T_d \approx 19$ K; see Figure 6), but warmer dust components (T_d up to 30 K) in compact and extended H II regions are evident at 70 μm.

Table 1
Data Sets Used

Instrument	Wavelength (μm)	FWHM (″)
PACS	70	5.2
PACS	160	12
SPIRE	250	18
SPIRE	350	25
SPIRE	500	37
GISMO	2 mm	21

In this paper we present the full 2 mm GISMO image of the Galactic center (Section 2). Here we concentrate on understanding the thermal emission from cold dust in molecular clouds that makes up the bulk of the emission seen at 2 mm. In Section 3 we describe the modeling of the *Herschel* far-IR observations of the CMZ region for the purpose of extrapolating this emission to 2 mm. The comparison of the extrapolated dust emission to the observed 2 mm emission provides a check on the inferred dust properties, temperature, and emissivity, and a means to separate 2 mm emission that arises from sources other than cold dust. The comparison between 2 mm free–free emission and thermal emission from dust allows us to make rough estimates of the gas density in regions where these components coexist (Section 4). Investigation of 2 mm emission from the brightest of the nonthermal radio filaments in the Galactic center is presented in a companion paper (Staguhn et al. 2019, Paper II).

2. Data and Resolution

2.1. GISMO

The 2 mm GISMO bolometric data were collected during 2012 April and November. A raster scanning pattern was used
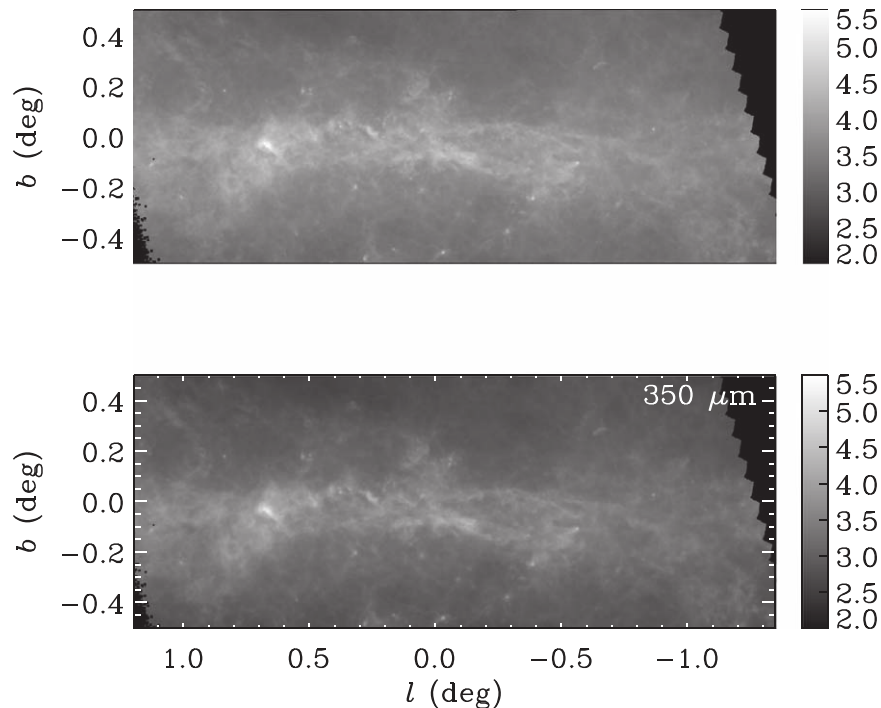
Figure 3. *Herschel* SPIRE 250 (top) and 350 μm (bottom) images from the Hi-GAL survey (Molinari et al. 2016). These are displayed on a logarithmic scale spanning [100, 3.5×10^5] MJy sr^{-1}. The 250 μm image is convolved to the 21″ resolution of the GISMO 2 mm data. Emission is dominated by cool dust ($T_d \approx 19$ K; see Figure 6).

for 52 separate scans that are combined here. The total observing time was approximately 8 hours and results in a median integration time of ∼1.1 s pixel^{-1}. Comprehensive Reduction Utility for SHARC-2 (CRUSH; version 2.22-b1) was used for the data reduction (Kovács 2008), employing the "faint" and "extended" processing flags and 40 "rounds" of iterations to help recover extended emission. The final image has a median noise level of 4.3 mJy beam^{-1}. The data reduction yields an image spanning roughly $1°.2 > l > -0°.8$ and $|b| < 0.3$, with an effective Gaussian beam of 21″ (FWHM). Although these data are collected from a single-dish telescope (not an interferometer), the data reduction necessitated some loss of large-scale structure due to the time-domain filtering required to remove atmospheric variations. There is also no measure of the absolute zero-point of the intensity. The GISMO data have been converted from the default units of Jy beam^{-1} to MJy sr^{-1} to facilitate comparison with the IR maps.

2.2. Herschel

The *Herschel* data used are data release 1 (DR1) data products, collected and processed as part of the the *Herschel* infrared Galactic Plane Survey (Hi-GAL) survey (Molinari et al. 2016). The data are broadband images from both the Photodetecting Array Camera and Spectrometer (PACS; Poglitsch et al. 2010) and The Spectral and Photometric Imaging Receiver (SPIRE; Griffin et al. 2010) instruments. The nominal wavelengths and angular resolution of the data are listed in Table 1. The data were obtained in seven separate fields from the archive[10] and rejoined together to cover the entire region observed by GISMO.

---

[10] http://vialactea.iaps.inaf.it/vialactea/eng/index.php

2.3. Convolution

To avoid artifacts in the modeling, we used the procedures of Aniano et al. (2011) to convolve all the images to a common resolution of 37″ (FWHM), which is limited by the 500 μm *Herschel* SPIRE data (see Table 1). For some later investigation of specific features in the 2 mm image, we convolved images to match GISMO's 21″ resolution. In such cases one must be cognizant of possible artifacts due to mismatched resolutions of the 350 and 500 μm data.

The Hi-GAL and GISMO images at 21″ resolution are shown in Figures 2–4. Figure 4 also shows the 19.5 cm radio continuum image of the region from Yusef-Zadeh et al. (2009), which reveals free–free and synchrotron emission.

3. Dust Emission Models

Inspection of Figure 4 shows that much of the 2 mm emission is correlated with far-IR (500 μm) emission. However, there are additional features in the 2 mm image that instead correlate with the radio (19.5 cm) emission. In order to characterize each of these emission components, we begin by constructing a model of the dust emission based on the far-IR *Herschel* data. This model can be used to predict and subtract the dust emission at 2 mm.

3.1. Far-IR Emission

The observed surface brightness, I_ν, of any pixel is given by

$$I_\nu = \int_0^{\tau_\nu} B_\nu(T_d') e^{-\tau_\nu'} d\tau_\nu', \qquad (1)$$

where $B_\nu(T_d')$ is the Planck function, T_d' and τ_ν' are the temperature and optical depth along the line of sight, and τ_ν is
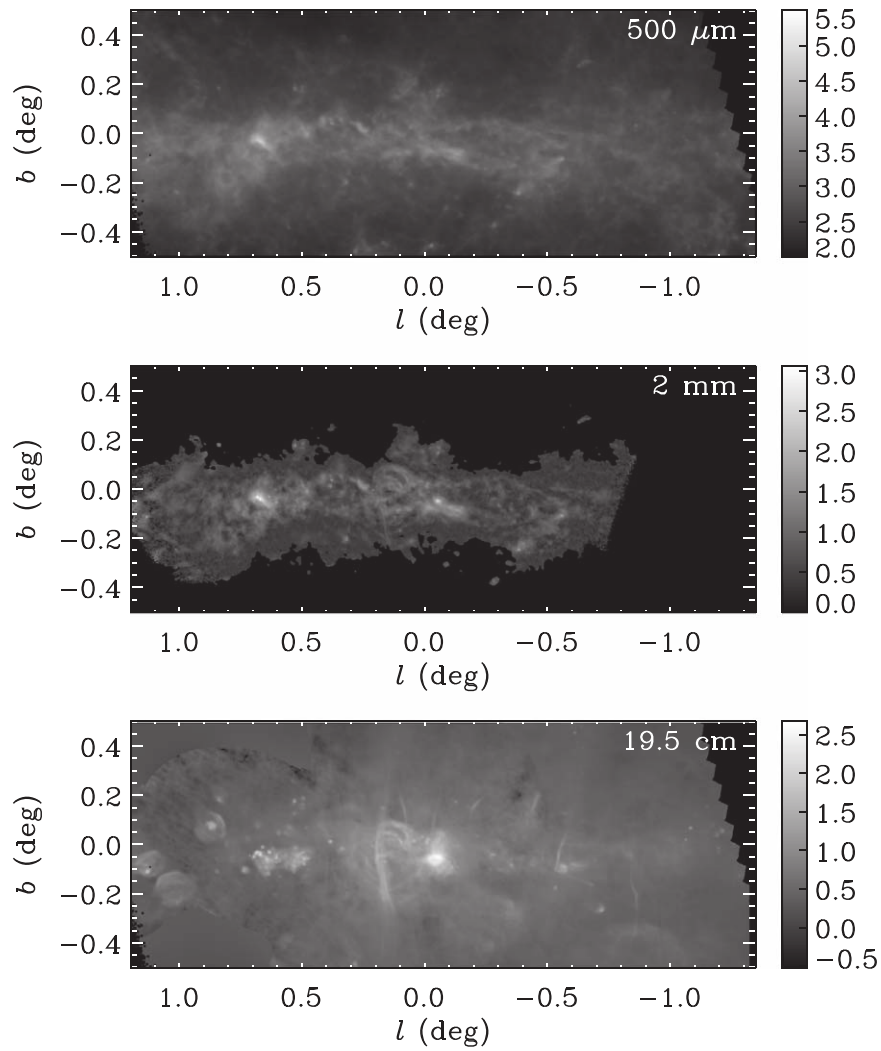
Figure 4. (Top) SPIRE 500 μm, (middle) GISMO 2 mm, and (bottom) VLA 19.5 cm images of the Galactic center region. These are displayed on a logarithmic scale spanning [100, 3.5 × 10^5], [1, 1150], and [0.3, 470] MJy sr^{-1}, respectively (an offset of +3 MJy sr^{-1} is applied to the 2 mm image to avoid truncating the negative noise variations of the background). The 19.5 cm image exhibits both thermal (free–free) and nonthermal (synchrotron) sources. The 2 mm image shows features in common with both longer- and shorter-wavelength images.

the total optical depth on the line of sight. Initial examination of the *Herschel* data indicated that the 160–500 μm data could generally be accurately fit if T'_d is taken to be constant (T_d) along the line of sight, while varying for each different line of sight. Therefore, we can model the emission as

$$I_\nu = B_\nu(T_d) \int_0^{\tau_\nu} e^{-\tau'_\nu} d\tau'_\nu, \quad (2)$$

$$= B_\nu(T_d)(1 - e^{-\tau_\nu}), \quad (3)$$

$$\approx B_\nu(T_d)\, \tau_\nu, \quad (4)$$

$$= B_\nu(T_d)\, \mathcal{M}_d\, \kappa_\nu. \quad (5)$$

With Equation (4) we assume $\tau_\nu \ll 1$, and then express the total optical depth in terms of the mass column density of the dust, $\mathcal{M}_d$, and the mass absorption coefficient of the dust, κ_ν. At long wavelengths, it is common to characterize the dust emissivity with a power law, such that $\kappa_\nu(\lambda) = \kappa_0\, \lambda^{-\beta}$.

Therefore, the model applied to fit the observed emission at $\lambda_i \in [160, 250, 350, 500]$ μm is

$$I_\nu(\lambda_i) = A\, B_\nu(T_d, \lambda_i)\, \lambda_i^{-\beta}, \quad (6)$$

where the parameters to be determined by χ^2 minimization are the dust temperature, T_d, the spectral index of the dust emissivity, β, and the normalization coefficient, A, which will be proportional to the product, $\mathcal{M}_d\, \kappa_0$. The fitting procedure integrates the model over the appropriate filter bandwidths before comparison to the observed intensities.

Figure 5 shows images of the dust temperature (T_d) and the dust emissivity index (β) as derived from these fits. The image of χ^2 of the fits is also shown. The image for the normalization (A) is very similar to that of $I_\nu(500\,\mu\text{m})$ and is omitted. On large scales, the derived dust temperature is higher than average in the vicinity of Sgr A and the Arches; it is lower than average in dense molecular clouds that are bright at 500 μm and are sometimes seen in extinction at 70 μm.
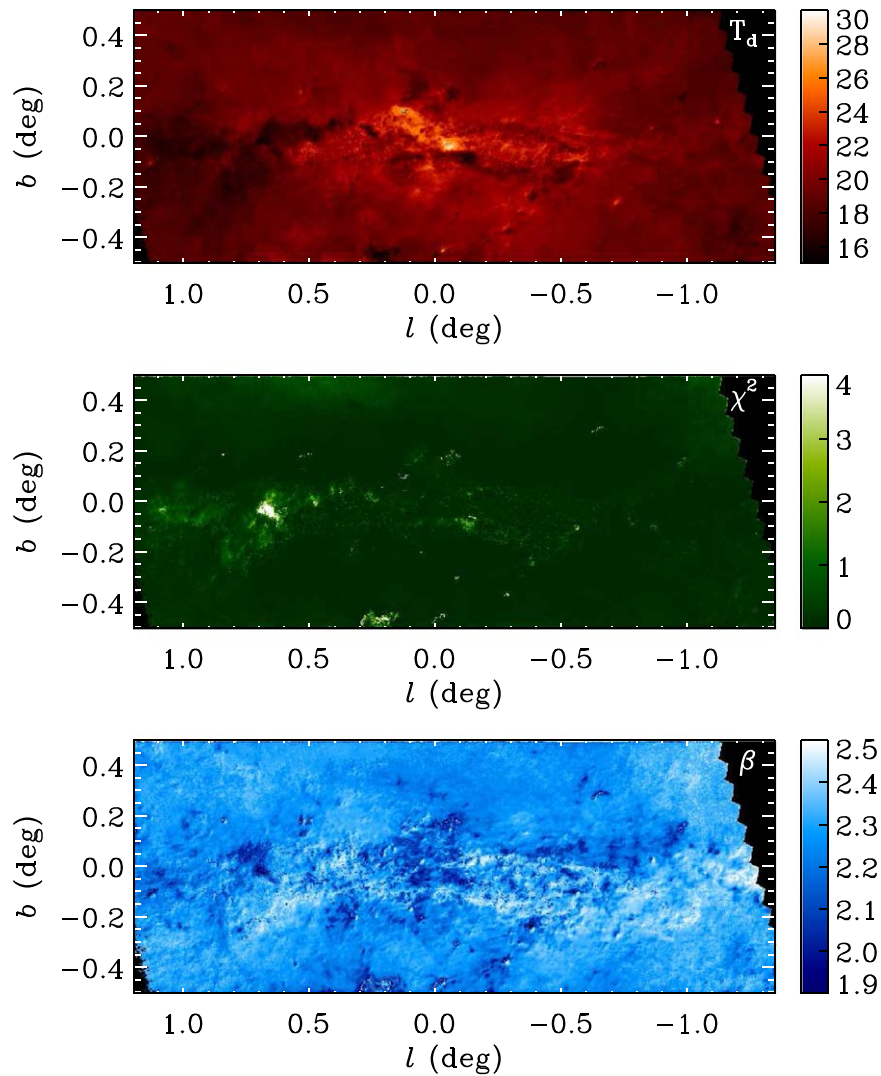
Figure 5. Modeling the 160–500 μm images using both dust temperature T_d (top) and β (bottom) as free parameters. The display ranges are [15, 35] for T_d and [1.9, 2.5] for β. The middle panel shows χ^2 for the fit at each pixel on a range of [0, 4] (fixed for comparison with later figures). Input data were convolved to 37″ resolution. T_d shows cold molecular clouds and warmer regions where strong local heating occurs. Results for β are more erratic and show spurious noise-induced features at the pixel scale.

Large scale variations in the spectral index are correlated with some features, but its not clear that consistent trends are present. Figure 6 shows a histogram of β that reveals that most of the data are consistent with a mean emissivity index of $\beta \approx 2.25$. A portion of the tails in the histogram, and some more extreme outliers, arise from scattered pixels where poor signal to noise in one or more bands leads to anomalous fits. Figure 7 shows that we find no strong correlation of T_d and β in this region. We do note that regions with $T_d \gtrsim 23$ K generally have lower β than most regions, although regions with relatively low β can be found at all temperatures. The maps in the middle and bottom panels of Figure 7 show that a relatively distinct clustering of points with high T_d and low β are mostly found in the vicinity of Sgr A and the Arches. Regions with low T_d and low β are mostly associated with molecular clouds such as the Sgr B2 complex.

Because of the occasionally spurious fitting results, we next investigated constrained fits where the emissivity index was fixed at $\beta = 2.25$. Figure 8 shows that the derived temperatures are similar to those found when β is a free parameter, but now there are no spurious pixel-to-pixel variations. The values of χ^2 increase somewhat, but there are few major changes. This constrained fit is used as our standard model in further analysis. The bottom panel in Figure 8 shows the dust mass surface density derived from the fit normalization A, assuming $\kappa_0 = 50$ cm^2 g^{-1} at $\lambda_0 = 100$ μm and that all the dust is at the Galactic center distance of 8.18 kpc (Abuter et al. 2019).

For comparison, we also performed a constrained fit using a more conventional value of $\beta = 2.0$. The temperature distribution (Figure 9) is very similar to that found for $\beta = 2.25$, except it is systematically slightly warmer, as would be expected for a flatter emissivity index. There are a few isolated regions where χ^2 is distinctly lower for the flatter spectral index. Many of these are associated with higher-latitude features that appear as IR dark clouds at shorter wavelengths ($\lambda \lesssim 70$ μm). The high latitude and extreme darkness of these
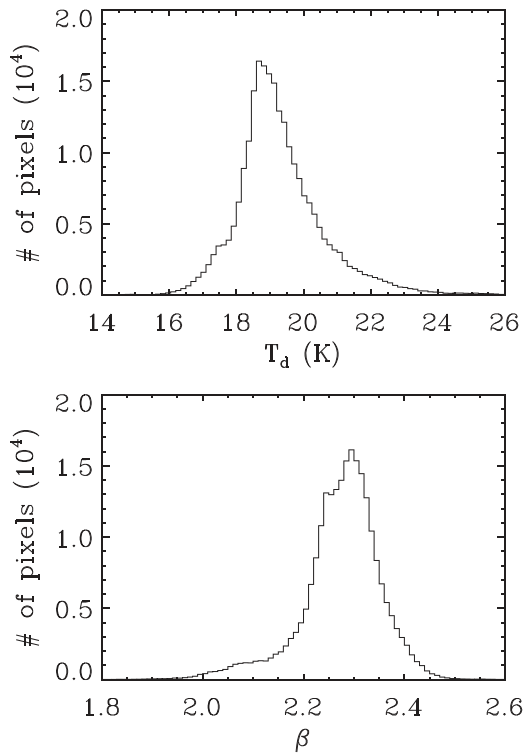
Figure 6. Histograms of the derived T_d (top) and β (bottom) for each pixel derived using the model in which both are free parameters (see Figure 5). The mean and median values of β are 2.27 and 2.28. Based on this distribution, we used a fixed $\beta = 2.25$ for subsequent models.

clouds suggest that they are in the foreground relative to the Galactic center.

There is a peculiar shell-like feature in the χ^2 map for $\beta = 2.0$ (Figure 9). It is 3′ in radius at $(l, b) = (359.65, +0.18)$ and is also distinguished from its surroundings by a slightly steeper value of $\beta \sim 2.35$ (Figure 5). Figure 10 provides a magnified view of this region. The structure is not particularly distinctive, but can be discerned, in the *Herschel* 160–500 μm intensity maps. The structure is not evident in *Spitzer* images at 3.6–24 μm or at radio wavelengths. While there are many possible candidates for a central star to this structure, none are particularly distinguished by exceptional colors or brightnesses at 1.25–24 μm.

3.2. 2 mm and 70 μm Emission

We extrapolate the emission model fit to the 160–500 μm data to predict the dust emission at 2 mm and at 70 μm. The extrapolated intensity maps are shown in Figure 11.

The observed 70 μm emission is always larger than the 70 μm intensity extrapolated from the model (Figure 12). The median ratio of the observed to predicted intensities is 2.1. The ratio tends to be higher in regions where the temperature is low, even though such regions can be optically thick at 70 μm and appear as IR dark clouds. The underestimate is likely due to two factors. The first is the neglect of a distribution of dust temperatures in the model. Warmer dust (either smaller dust and/or stochastically heated dust) will add intensity at the shorter wavelengths, broadening the spectrum. The second factor is the adoption of $\beta = 2.25$, which leads to a more sharply peaked spectrum than flatter values of the emissivity

index. While the steep index is found to fit the longer wavelengths, it is not necessary that this index continues to apply at shorter wavelengths. In either case, a more complete and physical model of the interstellar medium (ISM) emission would require additional parameters to fit the 70 μm data. However, at 160–500 μm wavelengths, the fit is already sufficiently good that additional parameters are not statistically warranted.

Despite the steep emissivity index, the model generally overestimates the 2 mm emission, especially in the cold dense molecular clouds of Sgr B2 and the Galactic center (Figure 13). However, there are many structures where the observed 2 mm emission is in excess of the extrapolated dust emission. These include extended and compact regions in Sgr B2, and Sgr B1; the Arches, Sickle, and Pistol Nebula; the Sgr A region; and other regions near Sgr C. Additionally, the brightest of the nonthermal filaments in the Galactic center is also evident, especially to the south of the Sickle Nebula. There is very weak evidence of emission from some of the other adjacent parallel filaments. However, none of the other nonthermal filaments are detected at other locations around the Galactic center.

4. Discussion

The far-IR spectral index of $\beta = 2.25$ derived here is steeper than would be expected for typical carbon grains ($\beta = 1$) or silicate grains ($\beta = 2$). However, the relatively high value of β is similar to that derived in other studies that fit for dust properties in selected areas or over the whole sky. For example, Planck Collaboration et al. (2014) used *Planck* observations at 30' resolution to fit dust emission over the whole sky. They found $\beta \approx 1.6$ at high Galactic latitudes ($|b| \gtrsim 10°$), but increasing to $\beta = 1.8$–2.0 in the inner Galactic plane ($|l| \lesssim 30$). Using 450 and 850 μm SCUBA observations of the CMZ combined with 100 μm IRAS data, Pierce-Price et al. (2000) found vales of $\beta \sim 2.4$ when β was allowed to be a free parameter of their model. Paradis et al. (2010) used *Herschel* data at 160, 250, 350, and 500 μm, and *IRAS* (*Interface Region Imaging Spectrograph*) 100 μm data (Miville-Deschênes and Lagache 2005) to model dust in two fields at $l = 30°$ and $l = 59°$. Their derived results at $l = 30°$ have a similar mean T_d and β as ours, but show a much stronger inverse correlation between these two parameters. The lack of correlation toward the Galactic center may be caused by more intrinsic variation in dust properties along longer lines of sight. The lack of spatial smoothness in the derived T_d and β (Figure 5), and the sometimes spurious results, may be the response to noise in the data when using χ^2 fitting methods (Juvela & Ysard 2012; Juvela et al. 2013).

The total dust masses within the 0.04, 0.08, and 0.3 $M_\odot$ asec^{-2} contours shown in Figure 8 are 4.3, 3.5, and $0.99 \times 10^5 M_\odot$ when 0.04 $M_\odot$ asec^{-2} is subtracted as background. With no background subtraction, the dust masses are 7.8, 4.6, and $1.05 \times 10^5 M_\odot$, and the total dust mass in the shown image is $1.3 \times 10^6 M_\odot$. Integrating the dust mass within the 0.08 $M_\odot$ asec^{-2} contour and where $0.75 > l > -0.65$ yields $2.4 \times 10^5 M_\odot$ over an area of 4.2×10^{-5} sr (consistent with the area and the $3 \times 10^7 M_\odot$ gas mass reported for the twisted ring structure by Molinari et al. 2011).

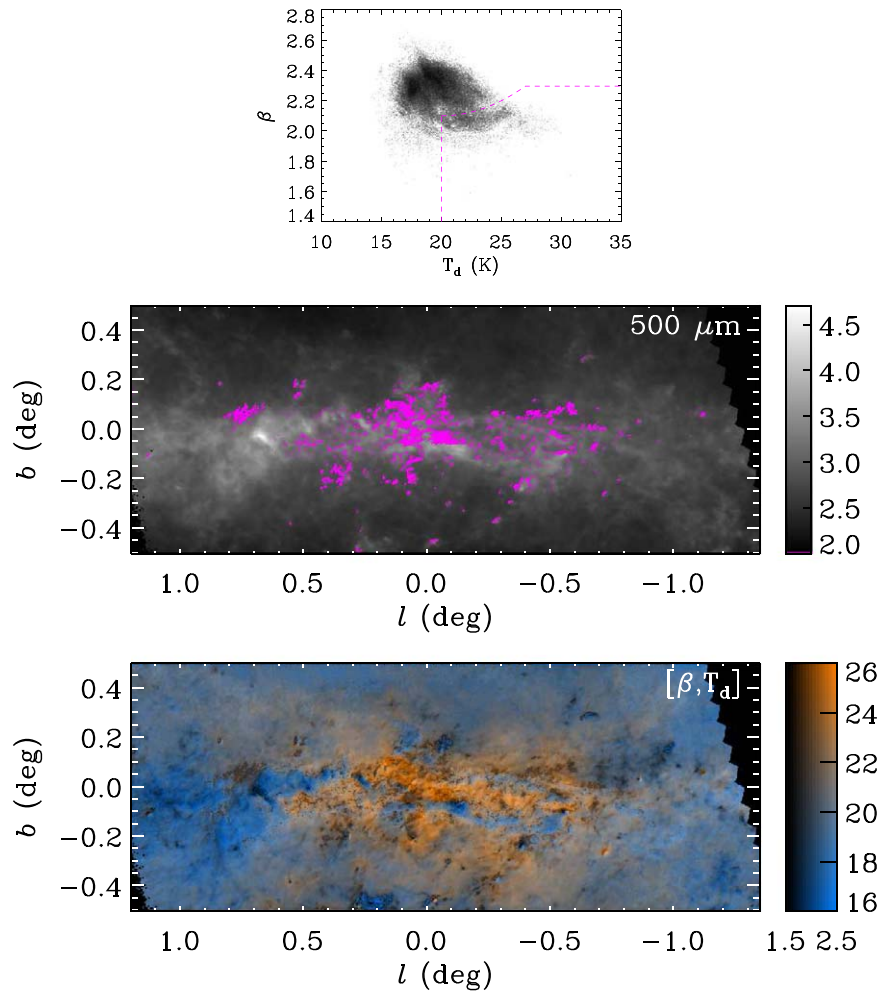It was expected that extrapolation of the single-temperature dust model to 70 μm would underestimate the emission in

Figure 7. The top panel shows a scatter plot between T_d and β for all pixels shown in Figure 5. There is no tight correlation between these parameters, although there is the loose trend that regions with high temperatures are likely to have relatively low values of β. The magenta line separates a branch of points with high T_d and low β whose locations are marked in magenta on the 500 μm image in the middle panel. The bottom panel shows the simultaneous distribution of T_d and β, encoding T_d with color from blue (cold) to orange (warm) and β with brightness from low (dark) to high (light) (see Figure 5).

star-forming regions where warm dust is common. This is indeed found in our modeling. However, underestimates also are unexpectedly found at the locations of IRDCs and other low-temperature regions (Figure 12). This result indicates that the 70 μm emission is coming from a substantially warmer dust component, possibly smaller or stochastically heated grains, or from warmer dust along the line of sight.

The extrapolation of the model to 2 mm shows that the observed emission can be brighter or fainter than the model prediction (Figure 13). The model tends to overpredict emission in the giant molecular clouds of Sgr B2, and the twisted ring of molecular clouds (Molinari et al. 2011). These are also well correlated with regions of low dust temperature, suggesting a value of $\beta > 2.25$ would be applicable to the colder clouds. This is weakly evident in the initial model that allowed a freely varying β, but is obscured by the overall noisiness of that unconstrained model (Figures 5 and 7). An additional contribution to overestimates of the 2 mm emission may be caused by missing large-scale structure in the GISMO image (Section 2.1), although the small scale of some

overestimated features indicates that this cannot be the sole explanation.

Finally, the real regions of interest are where there is 2 mm emission in excess of the model prediction. These regions are places where the 2 mm observations are sensitive to emission components other than the thermal emission from dust. For the most part, the excess regions correspond to the known star-forming regions and ionized structures in the Galactic center. The most prominent are Sgr A and its nearby H II regions Sgr A A-D (these four compact H II regions are not fully resolved from one another), the Arches, the Sickle and the Pistol Nebula, Sgr B1, and Sgr C. A large and bright region of excess emission is located around and to the south of the compact H II regions embedded in Sgr B2. Most surprisingly, there is excess 2 mm emission from the central filament of the Radio Arc. The emission extends southward from the vicinity of the Sickle and Pistol Star, $(l, b) = (0.16, -0.06)$, to a location near $(l, b) = (0.14, -0.21)$. The Radio Arc is the largest and brightest of the collection of nonthermal filaments that have been identified in the Galactic center. A detailed investigation
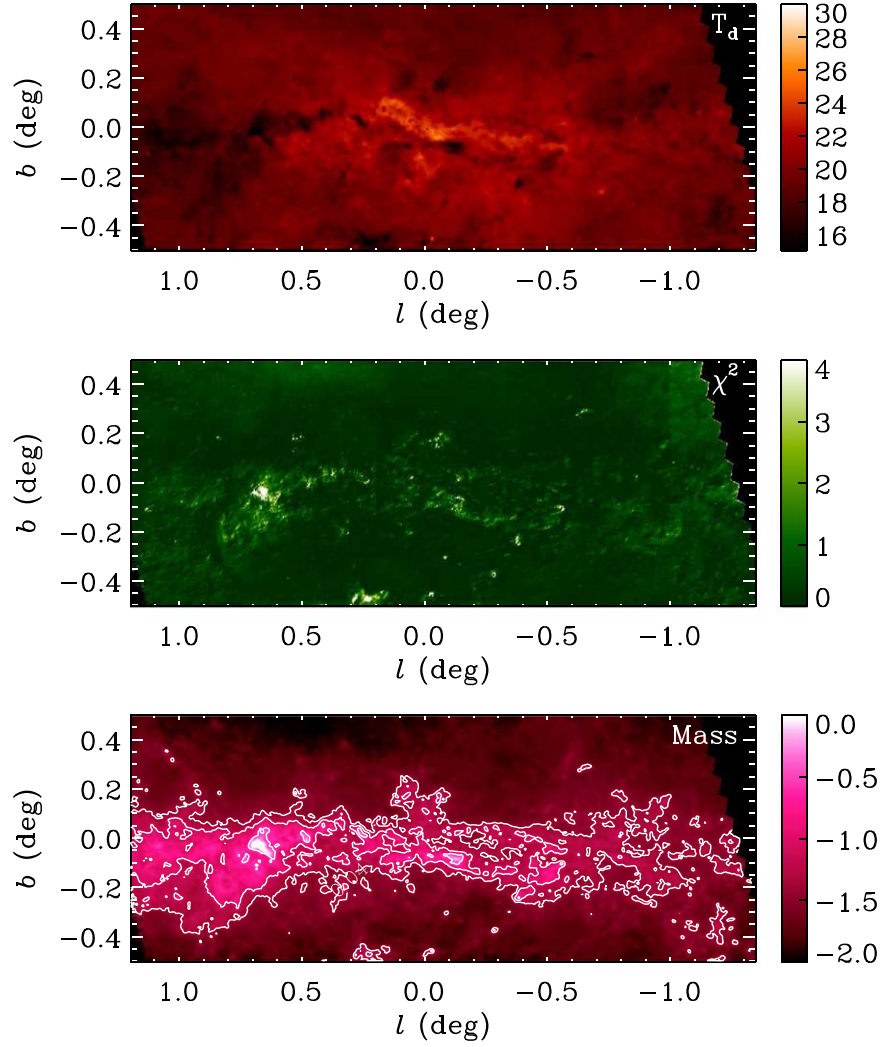
Figure 8. Modeling the 160–500 μm images using a free dust temperature T_d (top) but a fixed $\beta = 2.25$. The display range is [15, 35] for T_d. The middle panel shows χ^2 for the fit at each pixel on a range of [0, 4] (fixed for comparison with other figures). Input data were convolved to 37″ resolution. T_d is very similar to the case where β is a free parameter, except now all the variations are smoothly continuous without any spurious pixel-to-pixel variations caused by noise. χ^2 becomes worse at some locations (see Figure 5), as expected for a more constrained model. The bottom panel shows the model's dust mass surface density (proportional to the normalization parameter A). The image is logarithmically scaled from 0.01–1 $M_\odot$ asec^{-2}. Contours are at [0.04, 0.08, 0.3] $M_\odot$ asec^{-2}.

of this feature and the 2 mm emission from other non-dust sources is presented by Staguhn et al. (2019, Paper II).

In H II regions, the dust emissivity, $\epsilon_\nu^{IR}(\lambda)$, is given by

$$\epsilon_\nu^{IR}(\lambda) = 4n_d\, m_d\, \kappa(\lambda)\, \pi B_\nu(T_d, \lambda), \tag{7}$$

where n_d is the number density of dust grains, m_d is the mass of a single dust grain, $\kappa(\lambda)$ is the mass absorption coefficient for the dust, and $B_\nu(T_d, \lambda)$ is the Planck function evaluated at the dust temperature, T_d. Meanwhile, the free–free emissivity, $\epsilon_\nu^{ff}(\lambda)$, is given by

$$\epsilon_\nu^{ff}(\lambda) = C\, g_{ff}\, \frac{n_e\, n_i}{T^{0.5}\, e^{h\nu/kT}}, \tag{8}$$

where C is a numerical constant ($\approx 5.44 \times 10^{-41}$), g_{ff} is the gaunt factor, n_e and n_i are the number densities of electrons and ions, and T is the gas temperature. Thus, for a dusty region of ionized gas, the observed ratio, R, of 70 μm emission from

$T_d = 51$ K dust (Kaneda et al. 2012) to 2 mm free–free emission from $T = 10^4$ K gas can be used a rough diagnostic of the electron density via

$$R \approx 1.7 \times 10^6\, n_e^{-1}, \tag{9}$$

assuming a dust-to-gas mass ratio of $Z = 0.01$. If the gas temperature were instead taken to be 8000 K, then the electron density derived from the ratio of IR to free–free emission would increase by $\sim$10%. The coefficient in Equation (9) is much more sensitive to T_d, dropping by a factor of $\sim$70 if $T_d = 25$ K.

To employ this relation as a density diagnostic, we have plotted the 2 mm free–free emission (i.e., the residual after subtraction of the ISM dust contribution) against the 70 μm emission in Figure 14. We compare with the observed 70 μm emission, and with the emission after the subtraction of the extrapolated emission of cold dust component determined from the the 160–500 μm observations. The subtraction of this colder dust
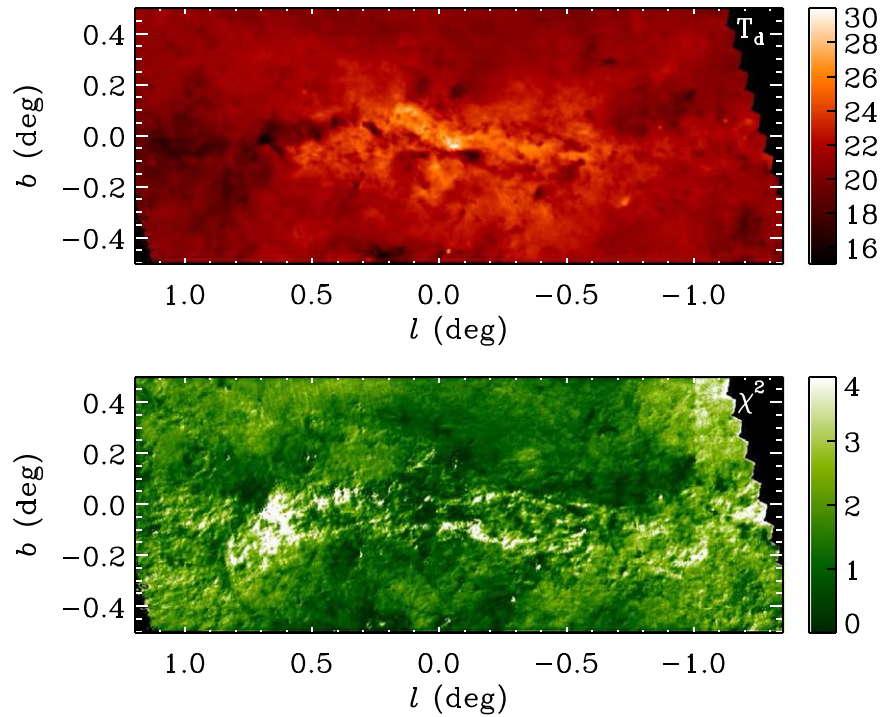
Figure 9. Modeling the 160–500 μm images using a free dust temperature $T_{\rm d}$ (top) but a fixed $\beta = 2.00$. The display range is [15, 35] for $T_{\rm d}$. The bottom panel shows χ^2 for the fit at each pixel on a range of [0, 4] (fixed for comparison with other figures). Input data were convolved to 37″ resolution. $T_{\rm d}$ is similar to, but systematically higher than, the case where $\beta = 2.25$. χ^2 is now much worse at all locations (see Figures 5 and 8), indicating that the *Herschel* data alone require $\beta > 2.0$. Curiously, it is in this χ^2 image that a circular feature at $(l, b) = (-0.35, 0.18)$ is most easily distinguished.
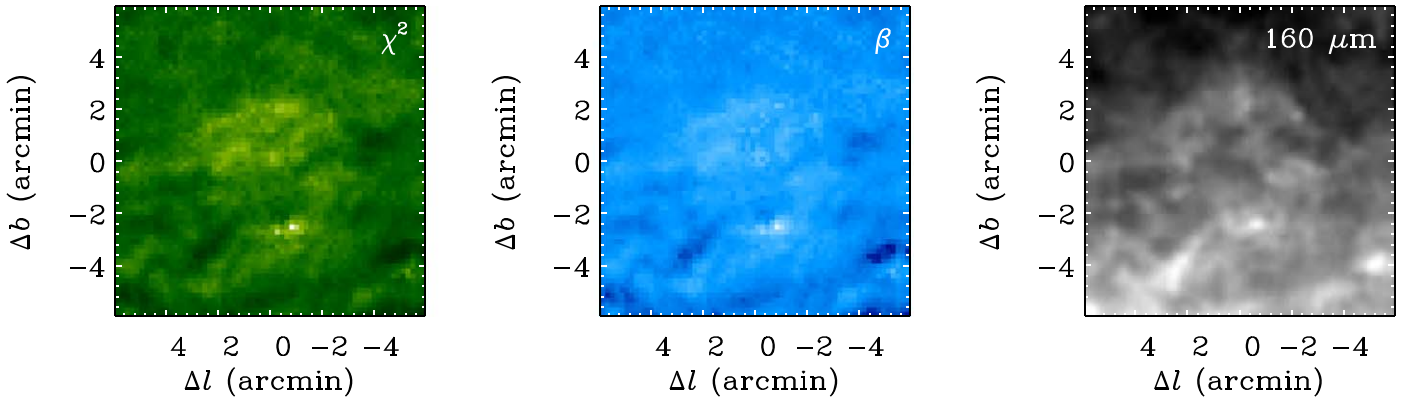

Figure 10. Magnified images of an unusual circular structure as revealed by fitting deviations (χ^2, left), emissivity index (β, middle), and 160 μm emission (right). The structure is centered at $(l, b) = (359.65, +0.18)$. The structure seems to be largely defined by unusual dust properties (see Section 3.1).

component is intended to better isolate the warmer emission from H II regions that produce the free–free emission. The comparison is limited to regions where $I_\nu(70\,\mu m) > 10^4$ MJy sr^{-1}, and where the residual $I_\nu(2\,mm) > 0$ MJy sr^{-1} after adjustment for the (negative) median background level. These scatter plots are shaded as a function of $n_{\rm e}$ as indicated by the diagonal lines. Figure 15 maps out the locations of the points in Figure 14 using the same color coding for the density $n_{\rm e}$. Without subtraction of the cold dust contribution at 70 μm, the relatively small variation in the selected 70 μm data means that the implied density is largely determined by the residual 2 mm brightness. For example the extremely bright regions in Sgr B2 imply the highest densities.

The less bright regions at Sgr B1, the Arches, and Sgr A have somewhat lower implied densities. If the extrapolated emission of the colder dust is subtracted from the 70 μm emission, the implied densities near Sgr B2 and Sgr A remain high, with a slight increase. Implied densities are more strongly increased for the fainter regions, which still exhibit large-scale structure though the structure is no longer directly correlated with the observed intensity.

Electron densities are more typically estimated from the ratios of ground-state fine-structure lines. Such determinations may be affected by extinction effects, but are only very weakly dependent on the gas temperature. Rodríguez-Fernández and
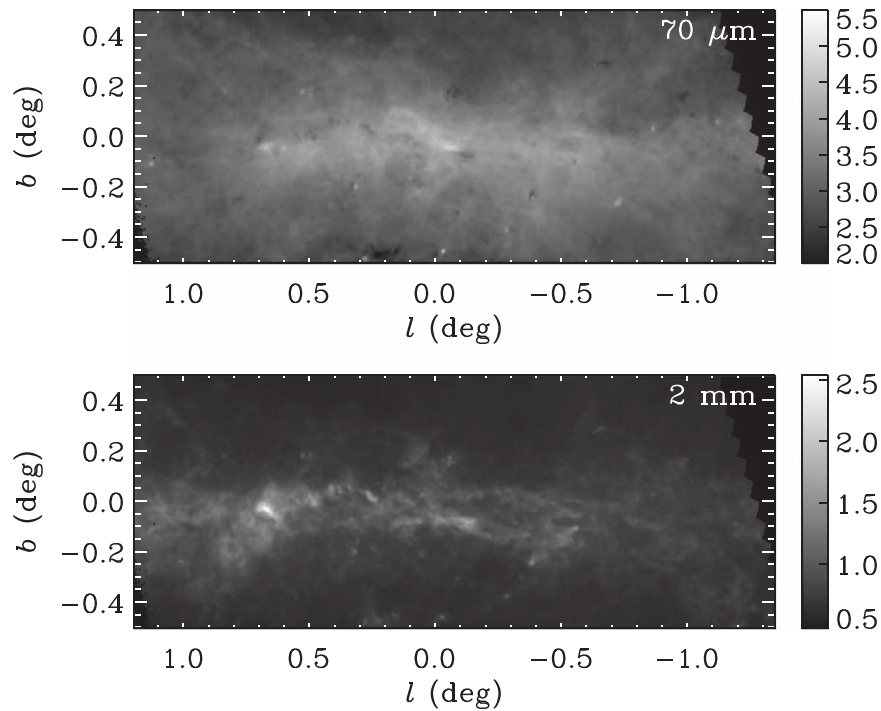
Figure 11. Images of 70 μm (top) and 2 mm (bottom) emission extrapolated from the fixed $\beta = 2.25$ model of the 160–500 μm emission. The data are convolved to 37″ resolution. These images are visually similar to the observed intensities shown in Figures 2 and 4, and are shown on the same logarithmic display ranges.
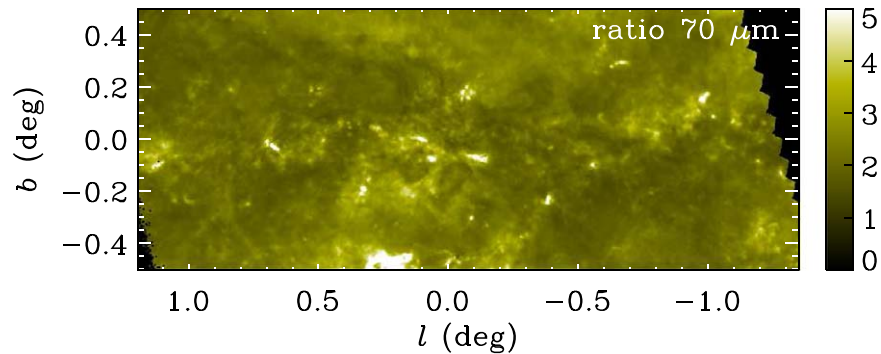

Figure 12. Ratio of observed to extrapolated 70 μm intensities (from Figures 2 and 11). The linear grayscale range is [0, 5]. White regions, where the observed 70 μm intensity is significantly greater than the extrapolated intensity, include star-forming regions with warm dust and, prominently, cold molecular clouds and infrared dark clouds (IRDCs).

Martín-Pintado (2005) derived $n_e < 30$–200 cm^{-3} from the [O III] 25/88 μm line ratios observed with the *Infrared Space Observatory* in several lines of sight in the CMZ. Simpson et al. (2018) used the Far Infrared Field-Imaging Line Spectrometer instrument on Stratospheric Observatory for Infrared Astronomy to observe this line ratio in the Sgr B1 region, finding $n_e \sim 300$ cm^{-3}, with some denser regions along some edges of Sgr B1. Using *Spitzer* observations of [S III] 18.7/33.5 μm line ratios, Simpson (2018) typically found $n_e \sim 300$ cm^{-3} in large regions across the CMZ, and $n_e \sim 300$–600 cm^{-3} across the Arches region in particular (Simpson et al. 2007). Direct comparison with the Arches results shows our densities are higher by factors of 1–10. Better agreement could be achieved by adjusting the estimates of one or more of the parameters in Equations (7) or (8), but without

further information it is impossible to judge which of the parameters should be adjusted.

5. Summary

GISMO 2 mm observations of the Galactic center are dominated by the thermal emission of dust in the general ISM and particularly in molecular clouds. We model the far-IR emission seen by *Herschel* in order to predict and remove dust emission from the 2 mm image. The dust temperature varies about a mean value of $T_d \approx 19$ K. Even though we find and set a relatively steep spectral index for the dust emission, $\beta = 2.25$, the 2 mm emission extrapolated from shorter-wavelength measurements is often overestimated for cold molecular clouds. This is consistent with previous studies finding an inverse correlation between spectral index and dust
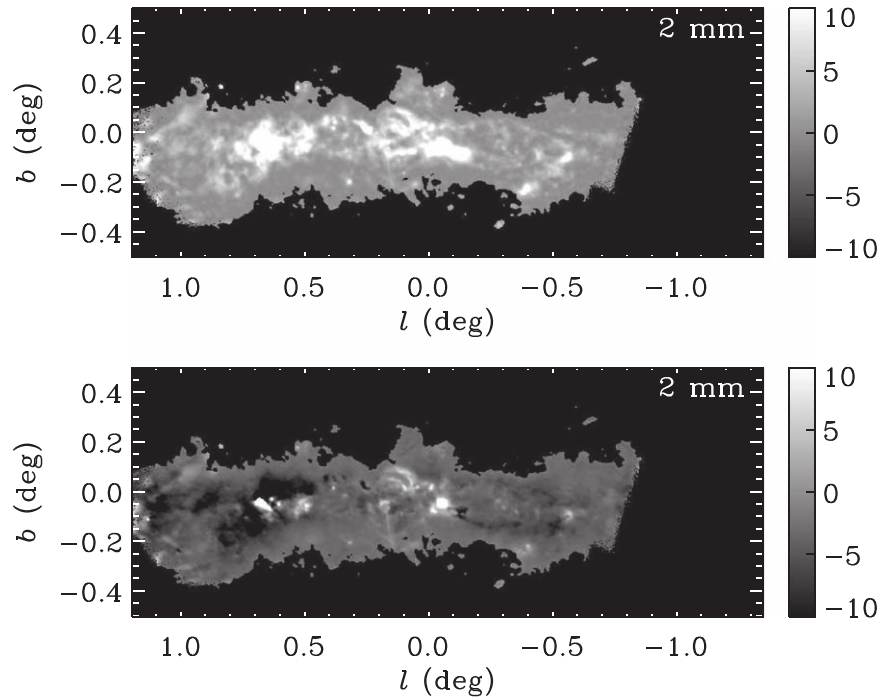
Figure 13. Observed 2 mm intensity (top) displayed on a linear grayscale range of $[-10, 10]$ MJy sr^{-1}, and the difference (bottom) between the observed and extrapolated 2 mm intensities on the same display range (37″ resolution). The difference image shows that most of the 2 mm emission is associated with thermal emission from dust. In regions where T_d is low, the emission is sometimes oversubtracted (appearing dark). Regions exhibiting 2 mm emission in excess of the dust emission (bright in the difference image) are H II regions and ionized structures that radiate via free–free emission at radio wavelengths, and nonthermal emission from the central filament of the Galactic center Radio Arc.
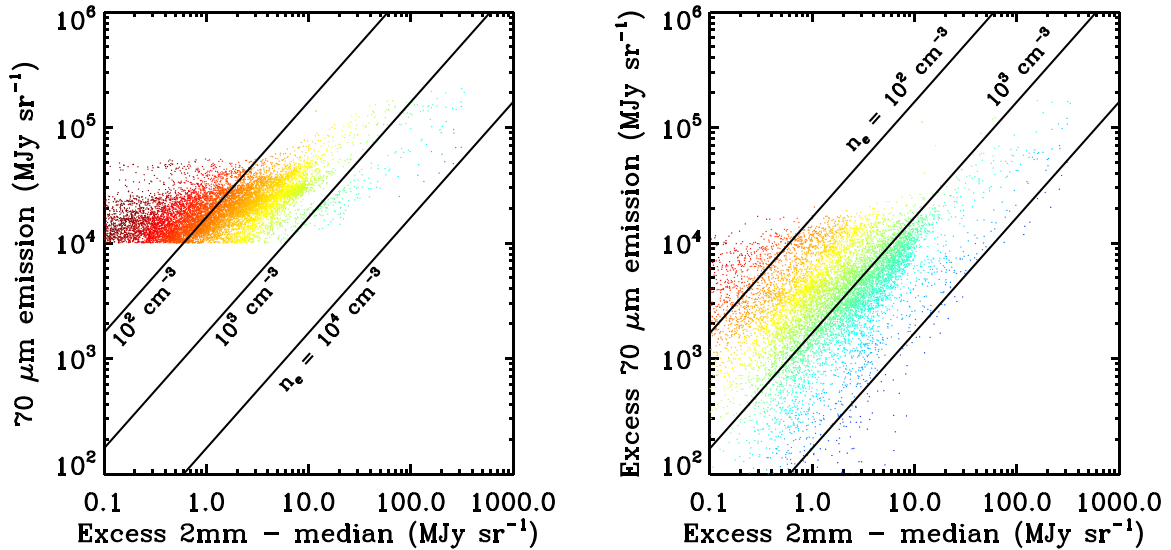

Figure 14. Ratio of residual 2 mm emission (mostly free–free) to 70 μm emission without (left) and with (right) subtraction of the emission of cold dust extrapolated from longer wavelengths. The points are shaded as a function of n_e, with several lines of constant density overplotted for guidance.

temperature. Star-forming regions and other ionized structures show additional 2 mm emission arising from the free–free mechanism. Nonthermal emission from the central filament of the Galactic center Radio Arc is also detected at 2 mm. This is the shortest wavelength at which this feature has been detected.
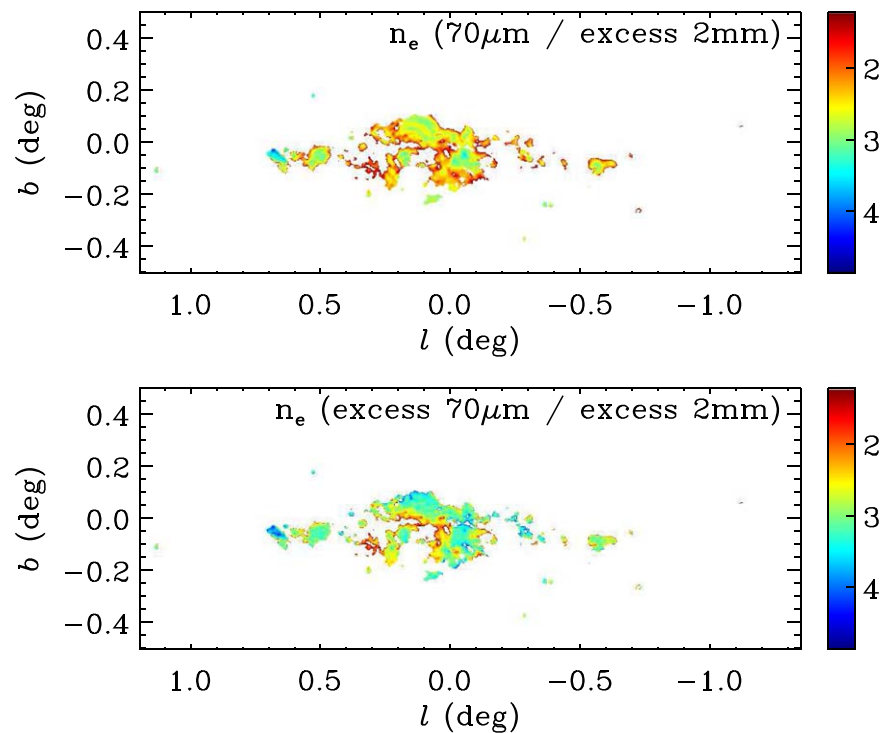
Figure 15. Maps of the logarithm of the electron density, $\log(n_e)$, implied by the ratio of residual 2 mm emission (mostly free–free) to 70 μm emission without (top) and with (bottom) subtraction of the emission of cold dust extrapolated from longer wavelengths. The latter case better isolates dust emission from warm regions where free–free emission is more likely to arise, and results in derived n_e values that are less correlated with the 70 μm brightness. The color scale for $\log(n_e)$ is the same as in Figure 14.

ORCID iDs

Richard G. Arendt ⓘ https://orcid.org/0000-0001-8403-8548
Johannes Staguhn ⓘ https://orcid.org/0000-0002-8437-0433
Eli Dwek ⓘ https://orcid.org/0000-0001-8033-1181
Mark R. Morris ⓘ https://orcid.org/0000-0002-6753-2066
Dominic J. Benford ⓘ https://orcid.org/0000-0002-9884-4206
Attila Kovács ⓘ https://orcid.org/0000-0001-8991-9088

References

Abuter, R., Amorim, A., Bauboeck, M., et al. 2019, A&A, 625, 10
Aniano, G., Draine, B. T., Gordon, K. D., & Sandstrom, K. 2011, PASP, 123, 1218
Baars, J. W. M., Hooghoudt, B. G., Mezger, P. G., & de Jonge, M. J. 1987, A&A, 175, 319
Bally, J., Aguirre, J., Battersby, C., et al. 2010, ApJ, 721, 137
Cotera, A. S., Colgan, S. W. J., Simpson, J. P., & Rubin, R. H. 2005, ApJ, 622, 333
Culverhouse, T., Ade, P., Bock, J., et al. 2010, ApJ, 722, 1057
Figer, D. F., McLean, I. S., & Morris, M. 1999, ApJ, 514, 202
Figer, D. F., Najarro, F., Gilmore, D., et al. 2002, ApJ, 581, 258
Genzel, R., Schödel, R., Ott, T., et al. 2003, ApJ, 594, 812
Ginsburg, A., Glenn, J., Rosolowsky, E., et al. 2013, ApJS, 208, 14
Griffin, M. J., Abergel, A., Abreu, A., et al. 2010, A&A, 518, L3
Juvela, M., Montillaud, J., Ysard, N., & Lunttila, T. 2013, A&A, 556, A63
Juvela, M., & Ysard, N. 2012, A&A, 541, A33
Kaneda, H., Yasuda, A., Onaka, T., et al. 2012, A&A, 543, A79
Kovács, A. 2008, Proc. SPIE, 7020, 70201S
Landsman, W. B. 1995, in ASP Conf. Ser. 77, Astronomical Data Analysis Software and Systems IV, ed. R. A. Shaw, H. E. Payne, & J. J. E. Hayes (San Francisco, CA: ASP), 437
Miville-Deschênes, M.-A., & Lagache, G. 2005, ApJS, 157, 302
Molinari, S., Bally, J., Noriega-Crespo, A., et al. 2011, ApJL, 735, L33
Molinari, S., Schisano, E., Elia, D., et al. 2016, A&A, 591, A149
Morris, M., & Serabyn, E. 1996, ARA&A, 34, 645
Paradis, D., Veneziani, M., Noriega-Crespo, A., et al. 2010, A&A, 520, L8
Pierce-Price, D., Richer, J. S., Greaves, J. S., et al. 2000, ApJL, 545, L121
Planck Collaboration, Abergel, A., Ade, P. A. R., et al. 2014, A&A, 571, A11
Planck Collaboration, Ade, P. A. R., Aghanim, N., et al. 2015, A&A, 580, A13
Poglitsch, A., Waelkens, C., Geis, N., et al. 2010, A&A, 518, L2
Pound, M. W., & Yusef-Zadeh, F. 2018, MNRAS, 473, 2899
Reich, W., Sofue, Y., & Matsuo, H. 2000, PASJ, 52, 355
Rodríguez-Fernández, N. J., & Martín-Pintado, J. 2005, A&A, 429, 923
Simpson, J. P. 2018, ApJ, 857, 59
Simpson, J. P., Colgan, S. W. J., Cotera, A. S., et al. 1997, ApJ, 487, 689
Simpson, J. P., Colgan, S. W. J., Cotera, A. S., et al. 2007, ApJ, 670, 1115
Simpson, J. P., Colgan, S. W. J., Cotera, A. S., Kaufman, M. J., & Stolovy, S. R. 2018, ApJL, 867, L13
Staguhn, J., Allen, C., Benford, D., et al. 2008, JLTP, 151, 709
Staguhn, J., Arendt, R. G., Dwek, E., et al. 2019, ApJ, 885, 72
Staguhn, J. G., Benford, D. J., Allen, C. A., et al. 2006, Proc. SPIE, 6275, 62751D
Wang, Q. D., Dong, H., & Lang, C. 2006, MNRAS, 371, 38
Wang, Q. D., Lu, F., & Lang, C. C. 2002, ApJ, 581, 1148
Yusef-Zadeh, F., Bushouse, H., Schödel, R., et al. 2015, ApJ, 809, 10
Yusef-Zadeh, F., Hewitt, J. W., Arendt, R. G., et al. 2009, ApJ, 702, 178